Published in final edited form as:
IEEE Trans Biomed Circuits Syst. 2009 ; 3(1): 1–10. doi:10.1109/TBCAS.2008.2005297.

Micropower CMOS Integrated Low-Noise Amplification, Filtering, and Digitization of Multimodal Neuropotentials

Mohsen Mollazadeh [Student Member, IEEE], **Kartikeya Murari [Student Member, IEEE]**, **Gert Cauwenberghs [Senior Member, IEEE]**, and **Nitish Thakor [Fellow, IEEE]**
M. Mollazadeh, K. Murari, and N. Thakor are with the Biomedical Engineering Department, Johns Hopkins University, Baltimore, MD 21205 USA (e-mail: mohsenm@jhu.edu; kartik@jhu.edu; nitish@jhu.edu)

G. Cauwenberghs is with the Division of Biological Sciences, University of California San Diego, La Jolla, CA 92093 USA (e-mail: gert@ucsd.edu)

Abstract

Electrical activity in the brain spans a wide range of spatial and temporal scales, requiring simultaneous recording of multiple modalities of neurophysiological signals in order to capture various aspects of brain state dynamics. Here, we present a 16-channel neural interface integrated circuit fabricated in a 0.5 μm 3M2P CMOS process for selective digital acquisition of biopotentials across the spectrum of neural signal modalities in the brain, ranging from single spike action potentials to local field potentials (LFP), electrocorticograms (ECoG), and electroencephalograms (EEG). Each channel is composed of a tunable bandwidth, fixed gain front-end amplifier and a programmable gain/resolution continuous-time incremental $\Delta\Sigma$ analog-to-digital converter (ADC). A two-stage topology for the front-end voltage amplifier with capacitive feedback offers independent tuning of the amplifier bandpass frequency corners, and attains a noise efficiency factor (NEF) of 2.9 at 8.2 kHz bandwidth for spike recording, and a NEF of 3.2 at 140 Hz bandwidth for EEG recording. The amplifier has a measured midband gain of 39.6 dB, frequency response from 0.2 Hz to 8.2 kHz, and an input-referred noise of 1.94 μV_{rms} while drawing 12.2 μA of current from a 3.3 V supply. The lower and higher cutoff frequencies of the bandpass filter are adjustable from 0.2 to 94 Hz and 140 Hz to 8.2 kHz, respectively. At 10-bit resolution, the ADC has an SNDR of 56 dB while consuming 76 μW power. Time-modulation feedback in the ADC offers programmable digital gain (1–4096) for auto-ranging, further improving the dynamic range and linearity of the ADC. Experimental recordings with the system show spike signals in rat somatosensory cortex as well as alpha EEG activity in a human subject.

Index Terms

Analog VLSI; biopotential amplifier; digital telemetry; electrocorticogram; electroencephalogram; local field potentials; micropower instrumentation; neural interface

I. Introduction

Advances in neuroscience research and clinical applications increasingly call for low-noise low-power integrated simultaneous recording of electrical potentials over large numbers of electrodes in the brain and the body. Implanted deep in the brain, these electrodes convey both high-frequency content of individual neuron action potentials (spikes), and lower-frequency content of local field potential (LFP) neural activity. Arrays of electrodes on the cortical surface or placed noninvasively on the scalp convey brain signals with further reduced frequency

content known as electrocorticograms (ECoG) and electroencephalograms (EEG), respectively.

Spike recordings usually convey the extracellular electrical activity of a single neuron unit. Depending on distance between the active neuron and the recording electrode, the amplitude of the extracellular spike signal is on the order of 500 μV and its frequency content ranges from 100 Hz to 7 kHz [1]. These recordings can be obtained using a single electrode or a microelectrode array [2]–[4]. LFPs are the result of collective synaptic activities of large assemblies of neurons around the recording electrode [5]. These signals may have amplitudes as high as 1 mV with frequency content up to 200 Hz [6]. LFPs may be recorded using the same electrodes as spikes. Electrical activity recorded from the surface of the brain (ECoG) or the scalp (EEG) using surface electrodes conveys brain wave signals that result from the volume conduction of coherent, collective neuronal activity over larger scales, throughout the brain. The power spectrum of EEG and ECoG signals is typically confined to 100 Hz and 200 Hz, respectively. The signal amplitude varies from 10 to 5000 μV for ECoG signals, and from 5 to 300 μV for EEG signals [7].

These various modalities of neural signals span a wide range of frequencies and amplitudes. Hence, an interface circuit for acquisition of biopotentials that can accommodate the above ranges and selectively isolate a signal of interest on demand, offers great advantages over an otherwise equally capable circuit confined to one specific signal modality. To be further useful, the system should also have low input-referred noise and should be able to remove the large dc offset on the signal due to the electrode-tissue interface without compromising the information-bearing low-frequency components of the signal. Over the years, several VLSI systems have been developed [8]–[23] to meet low noise and low power constraints imposed by the range of signal frequencies and amplitudes of interest to neuroscience and biomedicine. Typically the range of frequencies covered by any one of these systems is limited to one or two signal modalities, to accommodate high efficiency for the targeted application.

Harrison *et al.* [12] described a spike recording circuit with a bandwidth of 0.025 Hz to 7.2 kHz, input-referred noise of 2.2 μV_{rms} and power dissipation of 80 μW. A modified version of the circuit with a bandwidth of 30 Hz and power dissipation of 0.9, μW was also used as an EEG amplifier. Perelman *et al.* [17] reported a system which separates spikes from LFP after amplification. The amplifier has an input-referred noise of 3 μV_{rms} for a current consumption of 75 μA in the amplification stage. A biopotential acquisition system with a 57 nV/$\sqrt{\text{Hz}}$ input-referred voltage noise density and 60 μW power consumption capable of recording all biopotentials was reported by Yazicioglu *et al.* [20]. The amplifier uses a chopping technique to reduce the 1/f noise corner with a slight increase in power dissipation, and requires external components to implement highpass filtering. Lower power consumption with chopping for 1/f compensation is accomplished by adaptive feedback in the chopped signal [21]. A neural recording amplifier with two bandwidth settings for LFP and spike recording is reported in [22]. The design uses a folded cascode OTA in the input stage and has an input-referred noise of 3 μV_{rms} while consuming 7.56 μW of power from a 2.8 V supply.

Here, we present a 16-channel CMOS neural interface circuit with adjustable bandwidth, gain and resolution for the acquisition of biopotentials from the brain. The flexible design of the system and individual programmability of the channels enables capturing multimodal information across a wide frequency range of neural signals from spikes to EEG, while offering consistently low-noise and low-power performance over the range of frequency settings. For *in vivo* implantable instrumentation, the chip also includes digital readout in a bit-serial format compatible with wireless digital telemetry [24] as an alternative to analog wireless telemetry [25].

Section II describes the system architecture of the VLSI chip. Results of benchtop characterization and *in-vivo* recordings follow in Section III, and Section IV concludes the paper.

II. System Architecture

The neural biopotential interface circuit contains 16 parallel differential voltage input, serial digital output channels for acquisition of neurophysiological signals. Fig. 1 shows the block diagram of one channel. Each channel consists of a bandpass amplifier, a $G_m - C$ incremental $\Delta\Sigma$ ADC and decimation and readout circuitry. Two stages of gain are implemented in the system; a constant gain in the front-end amplifier, and a variable digital gain in the ADC stage. The amplifier's midband gain, $A_m = 100$ (40 dB), is set by the capacitor ratio $100C/C$, where C is 200 fF. Tunable filtering is incorporated in the amplifier stage itself. The low-end (highpass) cutoff frequency is set by the pseudo-resistive elements in the feedback loop (M_1 and M_2) and C as $1/2\pi RC$ where R is the resistance of M_1 and M_2 which is controlled by their gate voltage, V_{hpf} [26]. The high-end (lowpass) cutoff frequency is set by the unity gain frequency of the amplifier, f_u, and A_m as f_u/A_m. The high-end cutoff can be controlled by changing the g_m of the amplifier which results in a change in f_u.

The differential output voltage of the amplifier is then digitized by a 12-bit nominal, $G_m - C$ continuous-time, incremental $\Delta\Sigma$ ADC. The differential signal is first converted to a current by an operational transconductance amplifier (OTA). The difference between this current and the $\Delta\Sigma$ feedback current is then integrated on a capacitance C_{int} during the quantization cycle. The core of this ADC is a modified version of the ADC presented previously in [27]. This ADC structure was chosen for two reasons: because the continuous-time integration by the Gm-C input stage obliterates the need for sampling and thus for anti-alias filtering, and because the flexibility in choosing the number of bits allows optimal setting of resolution versus conversion bandwidth as dictated by the signals of interest; e.g., 7-bit at 16,000 samples/s for spikes and 12-bit at 500 samples/s for EEG recordings. The digital gain modulation implements duty cycle modulation in the $\Delta\Sigma$ current feedback, offering a precise and programmable digital gain between 1 and 4096. This gain modulation also decreases the quantization noise of the ADC since the input current is integrated over a longer time interval, albeit at the expense of a proportionally slower sampling rate. Thus, the system allows a configurable tradeoff between sampling rate and SNR. This along with the tunable filters allow the system to handle a wide gamut of neural signals from weak and slow (EEG, ECoG) to stronger and faster (spikes). In order to compensate for the inherent offset in the OTA stage, a charge pump circuit was added to nullify the output current of the OTA for zero input voltage. The control signal of the charge pump comes from the MSB of the digitized output such that when the bit is predominantly high (low), a respective dc current is added to (subtracted from) the output current of the OTA. This results in a midscale output of the ADC for a dc signal.

The digitized output then goes to the decimation and readout circuitry. The parallel-in serial-out circuitry of each channel is connected in a daisy chain fashion to the next channel in order to have a single-bit serial output. For benchtop characterization (Section III) this serial output was connected to a National Instruments DAQ data acquisition card to read the data into a computer.

A. Amplifier

The circuit diagram of the amplifier is shown in Fig. 2. The design is a two-stage fully differential voltage amplifier with independent common-mode feedback circuitry in each stage. The input transistors M_1 and M_2 were chosen as p-channel devices for lower 1/f noise. For balancing of the bias currents, transistors $M_1 - M_4$ and $M_5 - M_8$ are biased at currents $I_{biasp}/2$ and $I_{biasp}/8$, respectively. Exact matching of the differential pairs was not a consideration in

transistor sizing, since the amplifier offset along with the dc signal component is removed by the highpass filter surrounding the amplifier [12]. The maximum bandwidth is achieved by setting I_{biasp} to 8 μA. To maximize the gain, input transistors of both stages M_1, M_2 and M_5, M_6 are sized with large W/L to operate in the subthreshold region with this maximum bias current. The amplifier's unity-gain frequency f_u is given by $g_{m1}/2\pi C_c$ where C_c is 15 pF for a maximum f_u of 800 kHz.

A decrease in I_{biasp} results in a decrease in the unity gain frequency and hence the bandwidth of the amplifier while maintaining the input transistors in the subthreshold region. The additional transistors M_9 and M_{10} cancel the zero in the right hand plane of the frequency response. The amplifier was designed for a phase margin of 62°.

Common mode feedback circuitry (CMFB) was implemented in each stage in order to control the output levels independently. Circuit schematics for CMFB1 and CMFB2 are shown in Fig. 2. CMFB1 is designed to operate in the subthreshold region in order to minimize power consumption. The forward gain of the CMFB1 is also small enough not to cause instability in the amplifier. Since $M_{11} - M_{13}$ are in subthreshold

$$V_{cm1} = \max(V_{om}, V_{op}). \tag{1}$$

CMFB2 implements standard common-mode feedback circuitry [28]. The input transistors $M_{14} - M_{17}$ are sized with long geometry to maximize the operational linear range of the feedback circuitry.

Analysis of the input-referred thermal noise of this circuit results in:

$$\overline{v_n^2} = \frac{16kT}{3}\frac{1}{g_{m1}}\left(1 + \frac{g_{m3}}{g_{m1}} + \frac{g_{m5}+g_{m7}}{g_{m1}g_{m5}^2(r_{o1} \parallel r_{o3})^2}\right)\Delta f \tag{2}$$

where k is the Boltzman constant, T is the absolute temperature, and Δf is the bandwidth. The first two terms in the right-hand side of (2), proportional to $1 + g_{m3}/g_{m1}$, represent noise contributions from the first stage transistors, while the third term originates from the second stage. Since the third term is negligible, the bias current of the second stage was chosen to be smaller (1/8) than that of the first stage in order to conserve power while maintaining low noise operation. Also, $1/g_{m1}$ and g_{m3}/g_{m1} were kept small to minimize the input-referred noise, by sizing the input transistors to operate in the subthreshold region, maximizing their g_m/I_D ratio. Transistor pairs $M_1 - M_2$ and $M_5 - M_6$ are sized very wide (216 μ/1.8 μ and 18 μ/1.8 μ, respectively) while $M_3 - M_4$ and $M_7 - M_8$ are sized very long (3.6 μ/27 μ, and 3.6 μ/7.2 μ, respectively). A decrease in I_{biasp} results in higher thermal noise levels at a smaller bandwidth. Correspondingly, the total noise power, integrated over frequency, remains approximately constant. A decrease in V_{hpf} reduces the resistance and thus the thermal noise from the pseudo-resistor element, and also decreases the 1/f noise since it is filtered out to greater extent at higher low-end (highpass) cut-off frequency.

B. Continuous-time Gm-C Incremental ΔΣ

A dedicated ADC is provided for each channel, in order to bypass the need for multiplexing the amplifier outputs to a high speed ADC, thereby reducing the complexity and power consumption of the system. Fig. 3 shows the circuit schematic of the ADC. In order to digitize the differential output voltage of the amplifier, the amplified signals are first converted to a single ended current using a nMOS differential pair OTA which also removes any remaining

common mode signal. At the beginning of each conversion cycle, the output node the OTA is set to V_{mid} (intClk_1), the other plate of C_{int} is set to V_{mid} (intClk_1) and the high gain inverting amplifier is reset (intClk_{1e}). During the conversion cycle (intClk_2) the input current is integrated on capacitor C_{int}, changing V_{int}. Each period of the *dsClk*, V_{int} is compared to V_{mid} and a decision (**D**) is made. The comparator is implemented using a correlated double sampling scheme (CDS) to reduce the dominant 1/f noise. The decision bit and the clock signal *dsClk* control the time modulation feedback circuit which contributes either $\{+I_{ref}, -I_{ref}$ or $0\}$ to the input current. The digital gain, G, in the ADC is achieved by passing the feedback current for one clock cycle followed by $G-1$ clock cycles of shunting the feedback. The 1.5-bit effective DAC is realized by transistors M_7 and M_8. These transistors are sized large to improve matching of the reference currents across the channels. They are biased to be continuously active, rather than switched, to decrease the effect of charge injection.

In order to compensate for mismatch in the OTA and in the current feedback of the ΔΣ ADC, a second OTA pair is provided at the voltage-to-current conversion stage. The MSB from the decimator adjusts the direction of the offset current through an integrator implemented by charge pump CP and capacitor C_{off}, once every conversion cycle. Larger or more frequent updates allows for further filtering of the 1/f noise outside the signal band.

There are two main sources contributing to the noise of the ADC: the DAC quantization noise and the OTA thermal noise. The input-referred noise power from DAC reference can be written as [27]

$$\overline{v_{\mathrm{ref},n}^2}=\frac{1}{g_{m1}^2}\sum_{i=1}^{\mathrm{OSR}-1}\frac{\overline{i_{\mathrm{ref},n}^2}}{G^2\mathrm{OSR}^2} \tag{3}$$

where OSR is the oversampling ratio of the incremental ADC, the number of cycles required for data conversion. $I_{ref,n}$ can be written as

$$\overline{i_{\mathrm{ref},n}^2}=4kT\frac{2}{3}g_{m7}\Delta f \tag{4}$$

For the OTA, the input-referred noise power can be written as

$$\overline{v_{\mathrm{OTA},n}^2}=\frac{16}{3}kT\frac{1}{g_{m1}}\left(1+\frac{g_{m5}}{g_{m1}}\right)\Delta f. \tag{5}$$

Thus the total noise at the input of the continuous-time ADC is

$$\begin{aligned}\overline{v_{adc,n}^2}&=\overline{v_{\mathrm{OTA},n}^2}+\overline{v_{\mathrm{ref},n}^2}\\&\approx\frac{16kT}{3}\frac{1}{g_{m1}}\left(1+\frac{g_{m7}}{2g_{m1}G^2\mathrm{OSR}}\right)\Delta f\end{aligned} \tag{6}$$

The input referred noise of the ADC should be much smaller that the output noise of the amplifier. This can be achieved by increasing g_{m1}. However, the value of g_{m1} should not be chosen too large since that would decrease the operational range of the OTA. $M_1 - M_4$ were

sized 3.6 μ/54 μ for a I_{biasn} of 4 μA. An increase in digital gain, G, will result in a G^2-fold decrease in the second term of (6) without a change in the dynamic range of the ADC. The ADC was designed to have a linear range of 250 mV and digital gain was used to reduce the quantization noise.

The time modulation feedback is controlled by *dsClk*. The gain is introduced by programming the duty cycle of *dsClk*. The reference current is integrated only when *dsClk* is high while the input current is integrated during the whole period of *dsClk*. The duty cycle of *dsClk* represents the digital gain of the input current with respect to the reference current which can be set anywhere from 1 to 2^{12}. The integration period and the rate of sampling are set by int*Clk*, which is derived from *dsClk*. The clock signals intClk_1 and intClk_2 are nonoverlapping, derived from int*Clk*. Clock intClk_{1e} is a copy of int*Clk*1 with the rising edge following and the falling edge preceding those of intClk_1. The ratio of the periods of *dsClk* and int*Clk* determines the oversampling ratio OSR, ranging between 1 and 4096.

III. Experimental Results

The neural interface system was fabricated in a 0.5 μm 3M2P CMOS process through the MOSIS foundry service. The system was designed to run off a 3.3 V supply. The 16 channels occupy 3 mm × 3 mm of silicon area and consume 1.7 mW of power at the maximum bandwidth and speed. Fig. 4 shows the micrograph of the fabricated chip.

A. Benchtop Characterization

Fig. 5 shows the tunable amplifier's measured frequency response. The amplifier shows a midband gain of 39.6 dB, a maximum high-end cutoff frequency of 8.2 kHz, and a minimum low-end cutoff frequency of 0.2 Hz. The amplifier's bandwidth is adjusted in the 8.2 kHz–140 Hz range by varying I_{biasp} from 8 μA to 100 nA. The high-pass filter cutoff frequency can also be adjusted from 0.2 to 94 Hz by decreasing V_{hpf} from 1.65 to 1.25 V.

Fig. 6 shows the measured output noise power spectral density (PSD) of the amplifier for different I_{biasp} values. For I_{biasp} = 8 μA and V_{hpf} = 1.65 V, the amplifier shows a thermal noise level of 18 nV/√Hz and a 1/f corner frequency of approximately 1 kHz. A lower cutoff corner can be accomplished by chopping of the amplifier [20], [21], yielding further decreased noise power at some increase in circuit complexity and power consumption. Integration of the noise power spectral density from 0.5 Hz to 50 kHz, for the amplifier bandwidth setting of 8.2 kHz, gives an input-referred noise of 1.94 μV_{rms}. The noise efficiency factor (NEF) of the amplifier, a compound measure of noise performance and energy efficiency defined as [29]

$$\mathrm{NEF}=V_{n,\mathrm{rms}}\sqrt{\frac{2I_{\mathrm{total}}}{\pi\cdot U_T\cdot 4kT\cdot BW}} \tag{7}$$

yields 2.9 for the above settings, which compares favorably with NEF values between 3 and 10 reported in the literature (lower is better). As shown in Fig. 6, a decrease in I_{biasp} results in an increase of thermal noise floor of the amplifier and at the same time decreases the 1/f corner frequency and the bandwidth of the amplifier. For I_{biasp} = 100 nA and V_{hpf} = 1.65 V, integration of the noise spectral density of the amplifier from 0.5 Hz to 5 kHz for a bandwidth setting of 140 Hz yields an input referred noise of 1.65 μV_{rms}, and an NEF of 3.2. Fig. 7 compares the NEF of the amplifier of this work to that of previous designs [8]–[12], [14], [19]–[21]. As can be seen, the amplifier in this work compares favorably both at high and low bandwidth settings. The amplifier has a common-mode rejection ratio (CMRR) of more than 76 dB for signals

between 1 Hz and 10 kHz and an electrode offset of 50 mV. Power supply rejection ratio (PSRR) also measures above 70 dB for the same signal range. The amplifier's measured total harmonic distortion (THD) is below 1 % for signals as large as 9.4 mV_{pp} yielding in a dynamic range of 70 dB.

Fig. 8 shows the signal to noise-distortion ratio (SNDR) for the ADC operated at an oversampling rate OSR, = 2^{10}, and at gain settings $G = 1$ and $G = 2$. As shown, an increase in G results in improved performance of the ADC. This improvement owes to reduced switch injection noise with larger gain modulation (lower duty cycle of current feedback) [27]. For typical lower signal levels where the quantization noise is dominant, the SNDR increases by 3.5 dB with the two-fold increase in G. For large signal levels near the limit of the range, the SNDR saturates to 55 dB, limited by harmonic distortion. The integral non-linearity INL (differential nonlinearity DNL) of the ADC also decreases from 3 LSB (2.5 LSB)) for $G = 1$ and OSR = 2^{12}, to 1.5 LSB (1 LSB) for $G = 4$ and OSR = 2^{10}. Improvements in INL and DNL can be obtained by further increasing the digital gain G, at the expense of lower bandwidth.

Fig. 9 shows the power spectrum of the recorded digital output of one channel with a 1 mV_{pp} 50 Hz sine wave presented to the frontend amplifier input. The ADC was set for 10-bit resolution and $G = 1$. The resulting digital output showed a THD of 0.3 %. The output channel noise is 0.9 LSB (2.5 μV_{rms}) for these settings. ADC thermal noise and quantization noise contribute to this increased noise level with respect to the amplifier noise. Lower quantization noise levels can be attained by higher gain settings G for smaller signal amplitudes.

B. In-vivo Experiments

Spike recording was performed on 250 gram male Spargue-Dawley rats using a protocol approved by the Johns Hopkins Animal Care and Use Committee. Fig. 10 illustrates the experimental setup, and shows spike data from an anesthetized rat somatosensory cortex recorded on the system using a 1 MΩ tungsten electrode (FHC, ME). No significant difference was observed in comparison with similar recordings with a commercial acquisition device (Tucker Davis Technologies, FL). The system was also evaluated for recording of EEG signals from a human subject. The male subject was fitted with a 20-elec-trode cap with gel-based electrodes (Electro-Cap, OH) and the O1 electrode was connected to the biopotential ADC, sampling the signal at 250 Hz and digitizing the resulting data to 10-bit. Fig. 11 shows the power spectrum of the recorded signal, obtained when the subject closed the eyes. The resulting peak at 11 Hz in the spectrum clearly reveals recorded α-wave brain activity which is typical in the absence of visual stimulus [7]. A fragment of the raw recorded EEG waveform is also shown as an inset in the figure.

IV. Discussion and Conclusion

The presented neural interface system addresses an emerging need, both in biomedicine and systems neuroscience, for simultaneous recording of various modalities of neural signals including EEG, ECoG, LFP, and spikes. There has been considerable effort to make use of the different signal modalities to decode movement or movement intention [30]–[35]. For instance, Hochberg *et al.* [36] demonstrated control of a prosthetic device using an ensemble of neuronal activity recorded from the primary motor cortex. Scherberger *et al.* [37] reported that LFPs can be used to predict behavioral state. The flexibility of recording these different signal modalities within the same neural interface hardware has been lacking in today's integrated recording microsystems.

In this paper we presented a 16-channel 3 mm × 3 mm neural acquisition system-on-chip, fabricated in 0.5 μm CMOS technology, capable of recording neural signals of various amplitudes and frequencies. Tunable filters were embedded in the amplifier front-end stage in

order to selectively amplify the signal of interest. A two-stage voltage amplifier design with reduced current levels in the output stage, significantly lowered the current consumption of the front-end circuit, without affecting noise performance. The amplifier input referred noise across the frequency range is below 2 μV_{rms}. For EEG signals at the lowest bandwidth setting of 140 Hz, each channel consumes 22 μA of current. For spike signals at the highest 8.2 kHz bandwidth setting, each channel consumes 35 μA of current.

The gain-modulated incremental ADC in each channel provides additional control over signal quantization, that can be tailored to the signal of interest. Higher digital gain in the ADC stage provides higher signal amplification and lower quantization noise, at the expense of signal bandwidth. The individually configurable gain/resolution setting for each channel allows optimum quantization based on the dynamic range and the frequency content of each signal of interest. The flexibility in bandwidth, gain and quantization allows the system to acquire various neural signals as selected in software, rather than by physical modification of the hardware.

Despite the necessary tradeoffs in the design to accommodate the wide operating range of neural signals of interest, the system offers approximately constant noise efficiency factor (NEF ≈ 3) across the entire frequency range, where noise power density and power consumption scale with the bandwidth setting, through adjustments of bias levels in the amplifier and gain/resolution settings in the ADC. This scaling is advantageous to the different requirements for acquisition of different types of neural signals across the spectrum. As shown in Fig. 6, for high current bias (I_{biasp} = 8 μA), the thermal noise level and 1/f noise corner are at acceptable levels for spike recording which requires higher voltage scale (≈1 mV) and hence affords higher noise at high bandwidth setting (≈1 kHz). At the other end of the spectrum of neural signals, the low bandwidth setting (≈100 Hz) required for EEG acquisition (I_{biasp} = 100 nA) leads to an increase in the thermal noise density, but to a slight decrease in the rms noise because of the compound effect of lower bandwidth and decreased 1/f corner frequency (Fig. 6). The lower rms noise together with higher ADC resolution (by gain modulation *G*) afforded by the lower bandwidth setting support increased amplitude resolution as required for EEG signals (≈ 10 μV).

Benchtop characterization as well as *in vivo* testing were performed with this system. The recordings were comparable with those made by commercial devices, at significantly lower power consumption and smaller size. Other biopotential signals of interest, across the body, that are within the operating range of the chip include electromyograms (EMG) representative of muscle activity, electrooculograms (EOG) tracking eye motion, and electrocardiograms (ECG) conveying heart activity. For instance, monitoring EMG and EOG activity jointly with scalp EEG offers great improvements in specificity of noninvasive brain-machine interfaces [30], and further allows to compensate for various motion artefacts in reconstructed brain activity [38].

Table I summarizes the measured performance of the chip. To our knowledge, this is the only biopotential recording system reported to date capable of simultaneously acquiring, on a single microchip without external components, a wide range of neural signal modalities ranging from spike action potentials to EEG brain waves, where each channel of recording can be individually configured in-site for the signal of interest. Furthermore, the integrated system-on-chip is suitable for *in vivo* neural instrumentation in an implanted system, offering a digital output that is compatible with VLSI systems for digital telemetry and power harnessing. We expect these two attributes of the neuropotential recording chip to be of great use in understanding the mechanisms underlying brain function and information processing and propagation throughout the brain.

Acknowledgments

This work was supported in part by NIH/NIA 1R01AG029681, NIH MH062444-065296, and the Whitaker Foundation. Chips were fabricated through the MOSIS foundry service. This paper was recommended by Associate Editor K. Cheung.

The authors would like to thank N. Li, S. Acharya, and V. Aggarwal for valuable discussion and help in the experiments.

Biographies

Mohsen Mollazadeh (S'04) received his B.Sc. degree in electrical engineering from Sharif University of Technology, Tehran, Iran, in 2004 and the M.S. degree in biomedical engineering from Johns Hopkins University, Baltimore, MD, in 2006, where he is currently working towards the Ph.D. degree.

His research interests include mixed-signal VLSI systems for neural interface, telemetry in implantable systems and the neural mechanisms of dexterous movements.

Kartikeya Murari (S'02) received the B.Tech. degree in electrical engineering from the Indian Institute of Technology, Madras, India, in 2002 and the M.S. degree in biomedical engineering from Johns Hopkins University, Baltimore, MD, in 2004, where he is currently working towards the Ph.D. degree in biomedical engineering.

His research interests lie in mixed-signal VLSI design for biomedical applications in sensing, imaging and power management and in neuromorphic systems.

Gert Cauwenberghs (S'89-M'94-SM'04) received the M.Eng. degree in applied physics from University of Brussels, Belgium, in 1988, and the M.S. and Ph.D. degrees in electrical engineering from California Institute of Technology, Pasadena, in 1989 and 1994.

He is Professor of Biology and Bioengineering at University of California San Diego, where he co-directs the Institute of Neural Computation. Previously, he held positions as Professor of Electrical and Computer Engineering at Johns Hopkins University, Baltimore MD, and as Visiting Professor of Brain and Cognitive Science at Massachusetts Institute of Technology, Cambridge. His research interests are in advancing silicon adaptive microsystems to understanding of biological neural systems, and to development of sensory and neural

prostheses and brain-machine interfaces. He pioneered the design and implementation of highly energy efficient, massively parallel microchips that emulate function and structure of adaptive neural circuits in silicon. His previous contributions include micropower parallel silicon support vector machines for real-time adaptive pattern recognition, and acoustic microarrays for auditory separation and localization.

Dr. Cauwenberghs is a Francqui Fellow of the Belgian American Educational Foundation, and received the National Science Foundation Career Award in 1997, Office of Naval Research Young Investigator Award in 1999, and Presidential Early Career Award for Scientists and Engineers in 2000. He was Distinguished Lecturer of the IEEE Circuits and Systems Society in 2003–2004, and chaired its Analog Signal Processing Technical Committee in 2001–2002. He currently serves as Associate Editor for IEEE Transactions on Biomedical Circuits and Systems, and IEEE Transactions on Neural Systems and Rehabilitation Engineering. He is a Senior Editor for the IEEE Sensors Journal.

Nitish V. Thakor (S'78-M'81-SM'89-F'97) received the B.Tech. degree in electrical engineering from Indian Institute of Technology, Bombay, India, in 1974 and the Ph.D. degree in electrical and computer engineering from the University of Wisconsin, Madison, in 1981.

He served on the faculty of Electrical Engineering and Computer Science of the Northwestern University between 1981 and 1983, and since then he has been with the Johns Hopkins University, School of Medicine, Baltimore, MD, where he is currently serving as a Professor of Biomedical Engineering. He conducts research on neurological instrumentation, biomedical signal processing, micro and nanotechnologies, neural prosthesis, and clinical applications of neural and rehabilitation technologies. He has authored more than 160 peer-reviewed

publications on these subjects. Currently he directs the Laboratory for Neuroengineering and is also the Director of the NIH Training Grant on Neuroengineering. One of his current research projects, in collaboration with a multi-University consortium, funded by DARPA, is to develop a next generation neurally controlled upper limb prosthesis. He is actively interested in developing international scientific programs, collaborative exchanges, tutorials and conferences on Neuroengineering and Medical Microsystems.

Dr. Thakor is the Editor-in-Chief of IEEE Transactions on Neural and Rehabilitation Engineering. He is a recipient of a Research Career Development Award from the National Institutes of Health and a Presidential Young Investigator Award from the National Science Foundation. He is a Fellow of the American Institute of Medical and Biological Engineering and Founding Fellow of the Biomedical Engineering Society. He is also a recipient of the Centennial Medal from the University of Wisconsin School of Engineering, Honorary Membership from Alpha Eta Mu Beta Biomedical Engineering student Honor Society and Distinguished Service Award from IIT Bombay.

References

1. Najafi K, Wise K. An implantable multielectrode array with on-chip signal processing. IEEE J Solid-State Circuits Dec;1986 21(6):1035–1044.
2. Hoogerwerf A, Wise K. A three-dimensional microelectrode array for chronic neural recording. IEEE Trans Biomed Eng Dec;1994 41(12):1136–1146. [PubMed: 7851915]
3. Maynard EM, Nordhausen CT, Normann RA. The Utah intracortical electrode array: A recording structure for potential brain-computer interfaces. Electroenceph Clin Neurophysiol 1997;102(3):228–239. [PubMed: 9129578]
4. Vetter R, Williams J, Hetke J, Nunamaker E, Kipke D. Chronic neural recording using silicon-substrate microelectrode arrays implanted in cerebral cortex. IEEE Trans Biomed Eng Jun;2004 51(6):896–904. [PubMed: 15188856]
5. Buzsaki G. Large-scale recording of neuronal ensembles. Nat Neurosci 2004;7(5):446–451. [PubMed: 15114356]
6. Andersen RA, Musallam S, Pesaran B. Selecting the signals for a brain machine interface. Curr Opn Neurobiol 2004;14(6):720–726.
7. Webster, JG. Medical Instrumentation, Application and Design. New York: Wiley; 1998.
8. Dorman M, Prisbe M, Meindl J. A monolithic signal processor for a neurophysiological telemetry system. IEEE J Solid-State Circuits Jun;1985 SSC-20(6):1185–1193.
9. Metting van Ring A, Peper A, Grimbergen C. High-quality recording of bioelectric events. Med Biol Eng Comp 1990;29(5):389–397.
10. Ji J, Wise K. An implantable CMOS circuit interface for multiplexed microelectrode recording arrays. IEEE J Solid-State Circuits Mar;1992 27(3):433–443.
11. Martins R, Selberherr S, Vaz F. A CMOS IC for portable EEG acquisition systems. IEEE Trans Instrum Meas May;1998 47(5):1191–1196.
12. Harrison R, Charles C. A low-power low-noise CMOS amplifier for neural recording applications. IEEE J Solid-State Circuits Jun.;2003 38(6):958–965.
13. Mohseni P, Najafi K. A fully integrated neural recording amplifier with dc input stabilization. IEEE Trans Biomed Eng May;2004 51(5):832–837. [PubMed: 15132510]
14. Patterson W, Song Y, Bull C, Ozden I, Deangellis A, Lay C, McKay J, Nurmikko A, Donoghue J, Connors B. A microelectrode/microelectronic hybrid device for brain implantable neuroprosthesis applications. IEEE Trans Biomed Eng Oct.;2004 51(10):1845–1853. [PubMed: 15490832]
15. Liu W, Sivaprakasam M, Wang G, Zhou M, Granacki J, Lacoss J, Wills J. Implantable biomimetic microelectronic systems design. IEEE Eng Med Biol Mag May;2005 24(5):66–74. [PubMed: 16248119]

16. Sarpeshkar R, Wattanapanitch W, Rapoport B, Arfin S, Baker M, Mandal S, Fee M, Musallam S, Andersen R. Low-power circuits for brain-machine interfaces. Proc IEEE Int Symp Circ Sys (ISCAS'2007) 2007:2068–2071.
17. Perelman Y, Ginosar R. An integrated system for multichannel neuronal recording with spike/LFP separation, integrated A/D conversion and threshold detection. IEEE Trans Biomed Eng Jan;2007 54(1):130–137. [PubMed: 17260864]
18. Harrison RR, Watkins PT, Kier RJ, Lovejoy RO, Black DJ, Greger B, Solzbacher F. A low-power integrated circuit for a wireless 100-electrode neural recording system. IEEE J Solid-State Circuits Jan;2007 42(1):123–133.
19. Aziz J, Genov R, Derchansky M, Bardakjian B, Carlen P. 256-channel neural recording microsystem with on-chip 3-D electrodes. Proc Tech Dig, IEEE Int Solid-State Circuits Conf (ISSCC'2007) 2007:160–594.
20. Yazicioglu RF, Merken P, Puers R, Van Hoof C. A 60 μW 60 nV/$\sqrt{}$Hz readout front-end for portable biopotential acquisition systems. IEEE J Solid-State Circuits May;2007 42(5):1100–1110.
21. Denison T, Consoer K, Santa W, Avestruz AT, Cooley J, Kelly A. A 2 μW 100 nV/rtHz chopper-stabilized instrumentation amplifier for chronic measurement of neural field potentials. IEEE J Solid State Circuits Dec;2007 42(12):2934–2945.
22. Wattanapanitch W, Fee M, Sarpeshkar R. An energy-efficient micropower neural recording amplifier. IEEE Trans Biomed Circuits Syst Jun;2007 1(2):136–147.
23. Chestek C, Gilja V, Nuyujukian P, Ryu S, Shenoy K, Kier R, Solzbacher F, Harrison R. Hermesc: RF wireless low-power neural recording system for freely behaving primates. Proc IEEE Int Symp Circ Sys (ISCAS'2008) 2008:1725–1755.
24. Sauer C, Stanacevic M, Cauwenberghs G, Thakor N. Power harvesting and telemetry in CMOS for implanted devices. IEEE Trans Circuits Syst I: Reg Papers Dec;2005 52(12):2605–2613.
25. Mohseni P, Najafi K, Eliades SJ, Wang X. Wireless multichannel biopotential recording using an integrated FM telemetry circuit. IEEE Trans Neural Syst Rehab Eng Mar;2005 13(3):263–271.
26. Olsson I, Buhl RHD, Sirota A, Buzsaki G, Wise K. Band-tunable and multiplexed integrated circuits for simultaneous recording and stimulation with microelectrode arrays. IEEE Trans Biomed Eng Jul; 2005 52(7):1303–1311. [PubMed: 16041994]
27. Stanacevic M, Murari K, Rege A, Cauwenberghs G, Thakor N. VLSI potentiostat array with oversampling gain modulation for wide-range neurotransmitter sensing. IEEE Trans Biomed Circuits Syst Feb;2007 1(1):63–72.
28. Johns, DJ.; Martin, K. Analog Integrated Circuit Design. New York: Wiley; 1997.
29. Steyaert M, Sansen W. A micropower low-noise monolithic instrumentation amplifier for medical purposes. IEEE J Solid-State Circuits Dec;1987 22(6):1163–1168.
30. Wolpaw JR, Birbaumer N, McFarland DJ, Pfurtscheller G, Vaughan TM. Brain—Computer interfaces for communication and control. Clin Neurophysiol 2002;113(6):767–791. [PubMed: 12048038]
31. Sanes JN, Donoghue JP. Oscillations in local field potentials of the primate motor cortex during voluntary movement. Proc Nat Acad Science 1993;90(10):4470–4474.
32. Heldman D, Wang W, Chan S, Moran D. Local field potential spectral tuning in motor cortex during reaching. IEEE Trans Neural Sys Rehab Eng Feb;2006 14(2):180–183.
33. Leuthardt EC, Schalk G, Wolpaw JR, Ojemann GJ, Moran DW. A brain-computer interface using electrocorticographic signals in humans. J Neural Eng 2004;1(2):63–71. [PubMed: 15876624]
34. Miller KJ, Leuthardt EC, Schalk G, Rao RPN, Anderson NR, Moran DW, Miller JW, Ojemann JG. Spectral changes in cortical surface potentials during motor movement. J Neurosci 2007;27(9):2424–2432. [PubMed: 17329441]
35. Stark E, Abeles M. Predicting movement from multiunit activity. J Neurosci 2007;27(31):8387–8394. [PubMed: 17670985]
36. Hochberg LR, Serruya MD, Friehs GM, Mukand JA, Saleh M, Caplan AH, Branner A, Chen D, Penn RD, Donoghue JP. Neuronal ensemble control of prosthetic devices by a human with tetraplegia. Nature 2006;442(13):164–171. [PubMed: 16838014]
37. Scherberger H, Jarvis MR, Andersen RA. Cortical local field potential encodes movement intentions in the posterior parietal cortex. Neuron 2005;46(2):347–354. [PubMed: 15848811]

38. Jung TP, Makeig S, Humpries C, Lee TW, Iragui MMJV, Sejnowski T. Removing electroencephalographic artifacts by blind source separation. Psychophysiology 2000;37:163–178. [PubMed: 10731767]

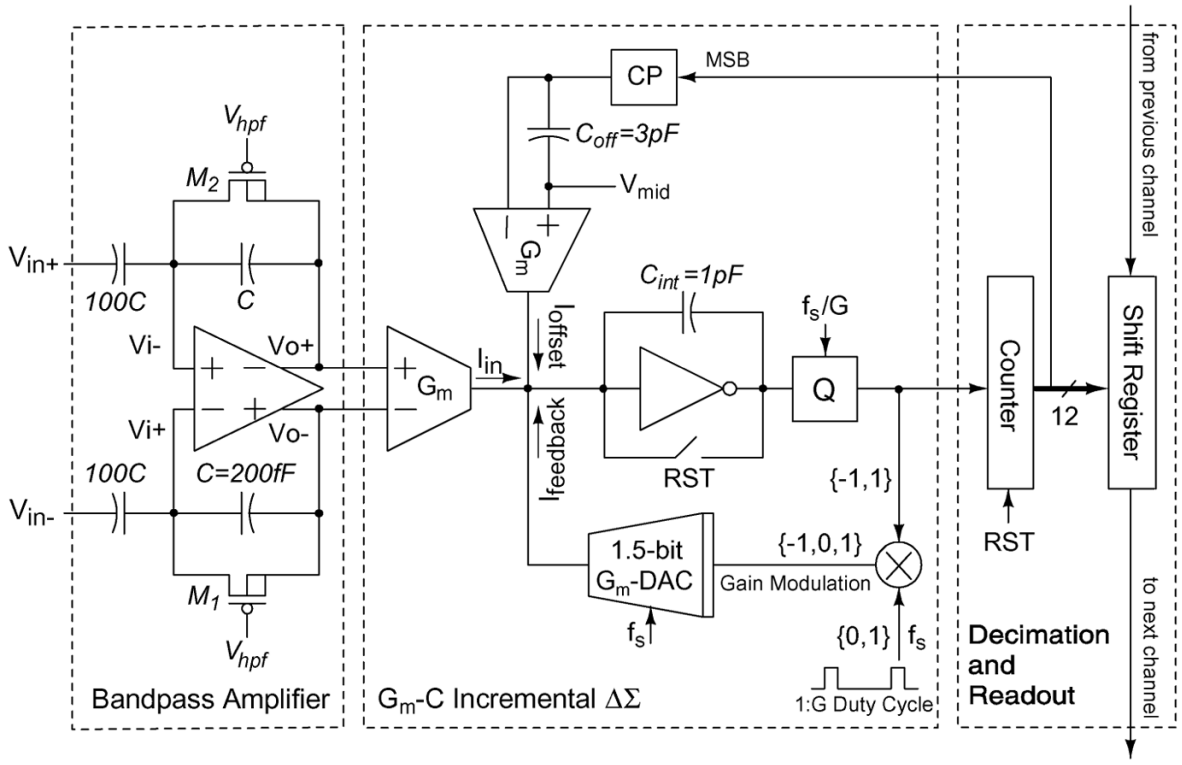

Fig. 1.
Functional block diagram for one channel of the 16-channel biopotential ADC.

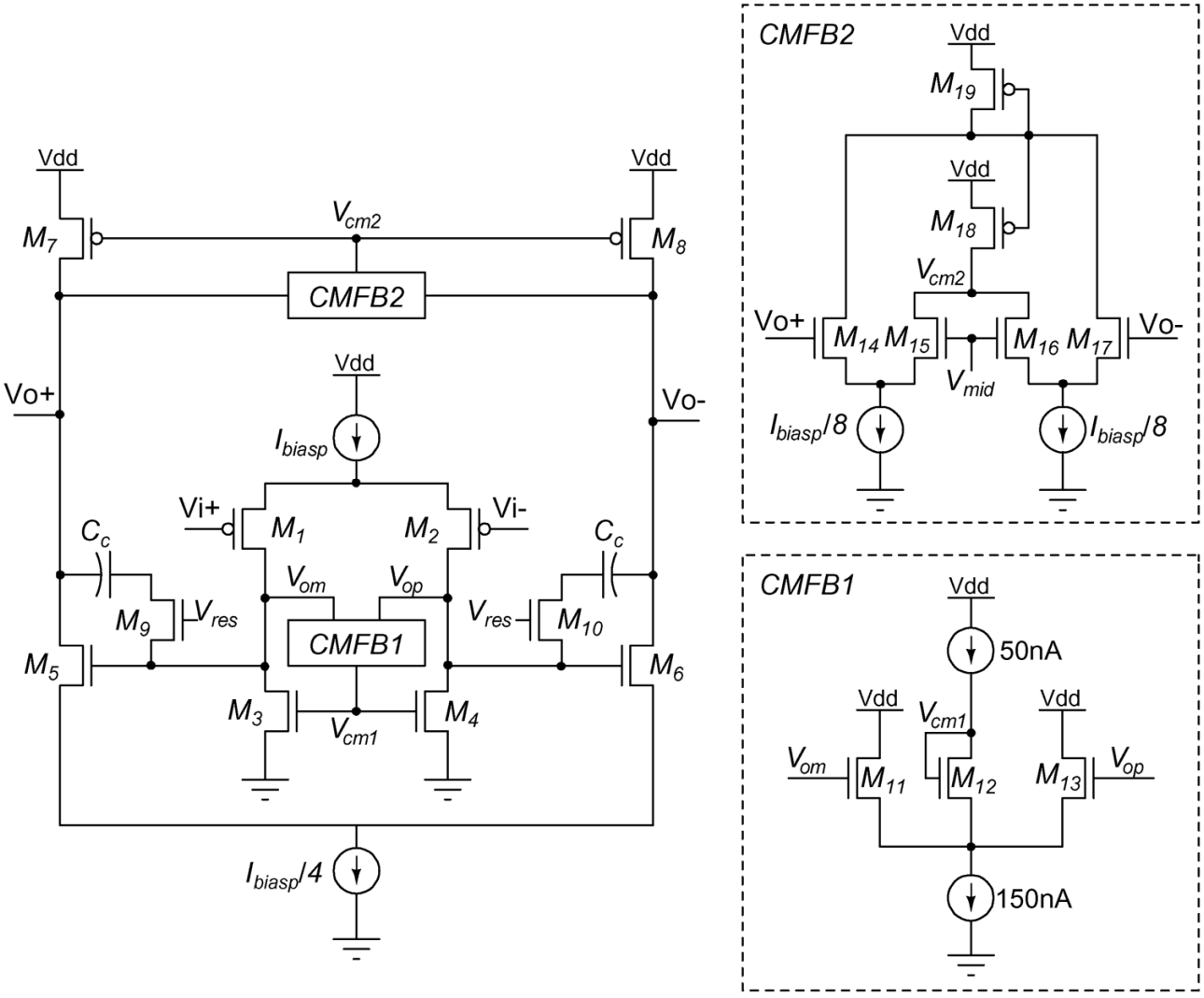

Fig. 2.
Fully differential two-stage amplifier in the bandpass amplifier frontend of Fig. 1.

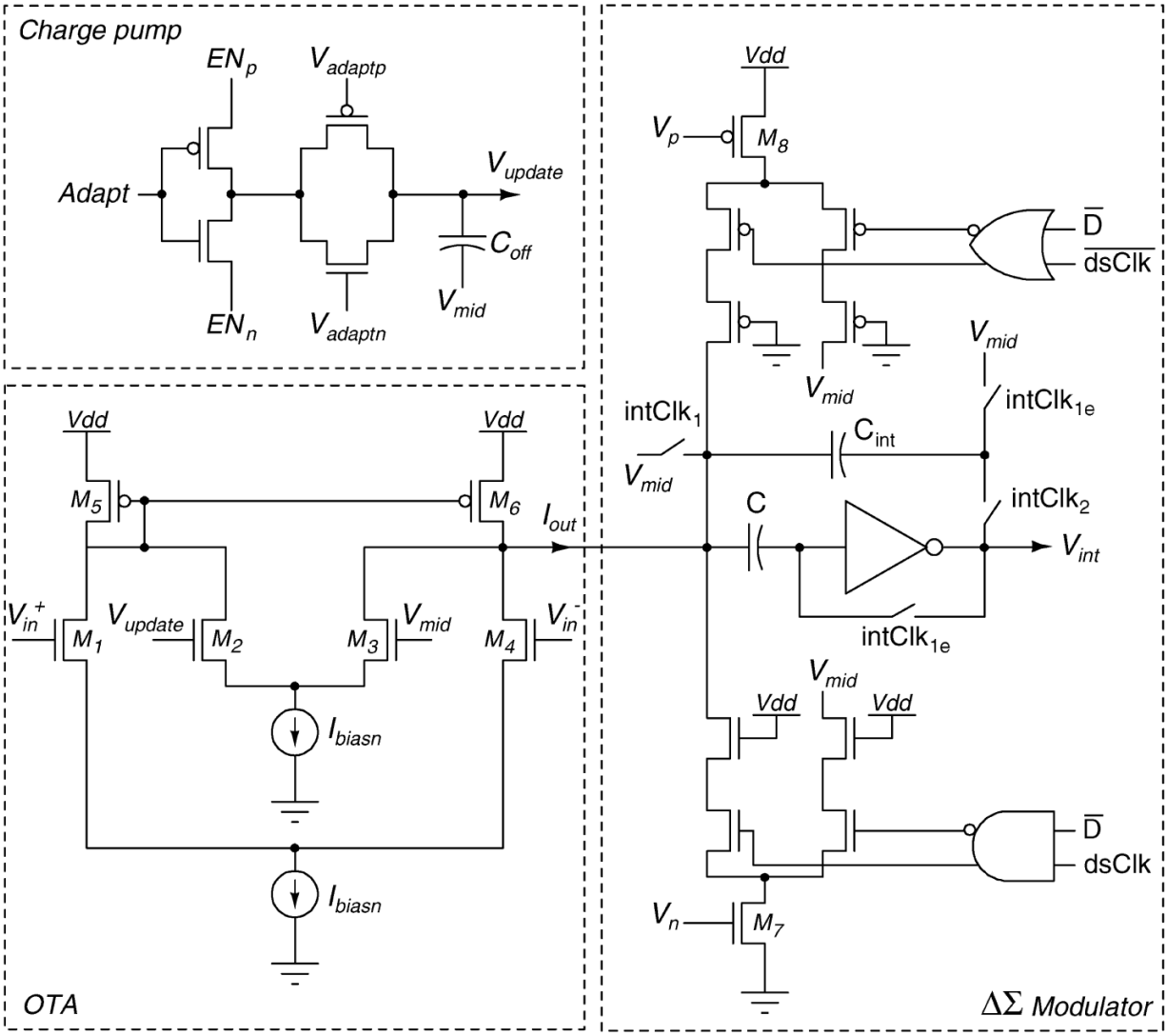

Fig. 3.
Circuit schematic of the continuous-time Gm-C incremental ΔΣ ADC, including adaptive offset cancelation.

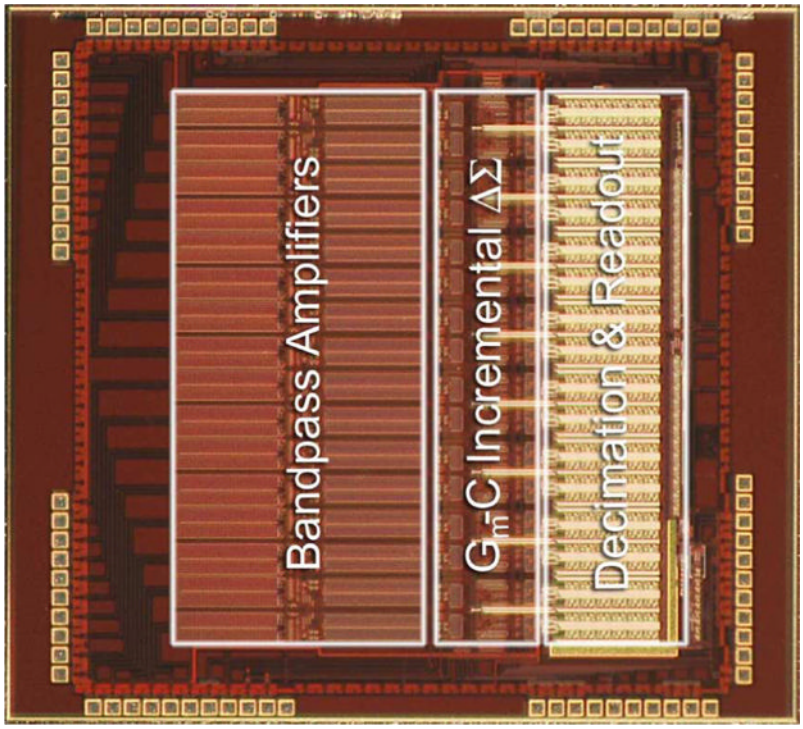

Fig. 4.
Micrograph of the fabricated chip. Die size is 3 mm × 3 mm in 0.5 μ3M2P CMOS technology.

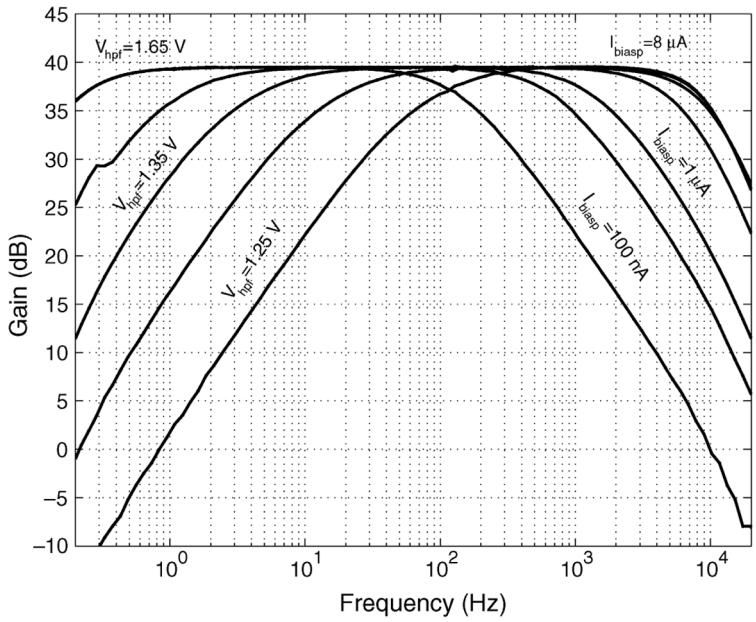

Fig. 5.
Filter response for lowpass current bias I_{biasp} between 100 nA and 8 μA, and for highpass voltage bias V_{hpf} between 1.25 and 1.65 V.

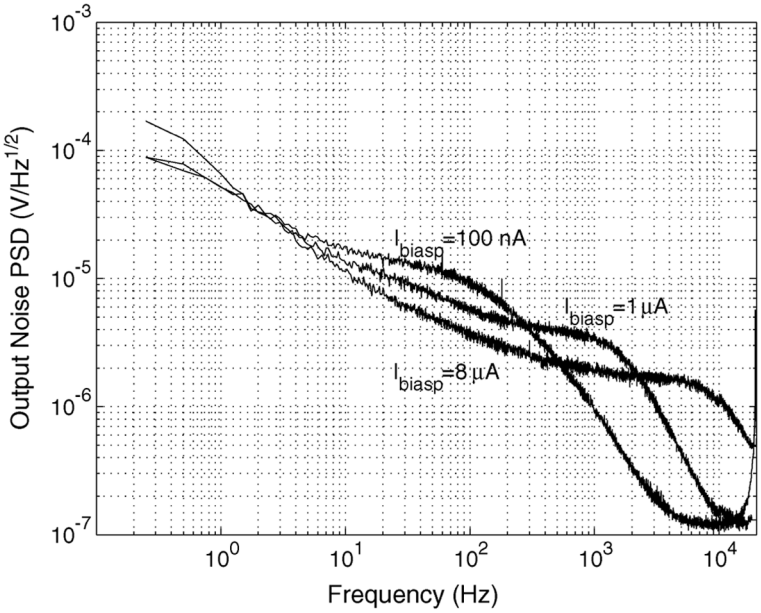

Fig. 6.
Measured output noise density of the amplifier for different bias I_{biasp}.

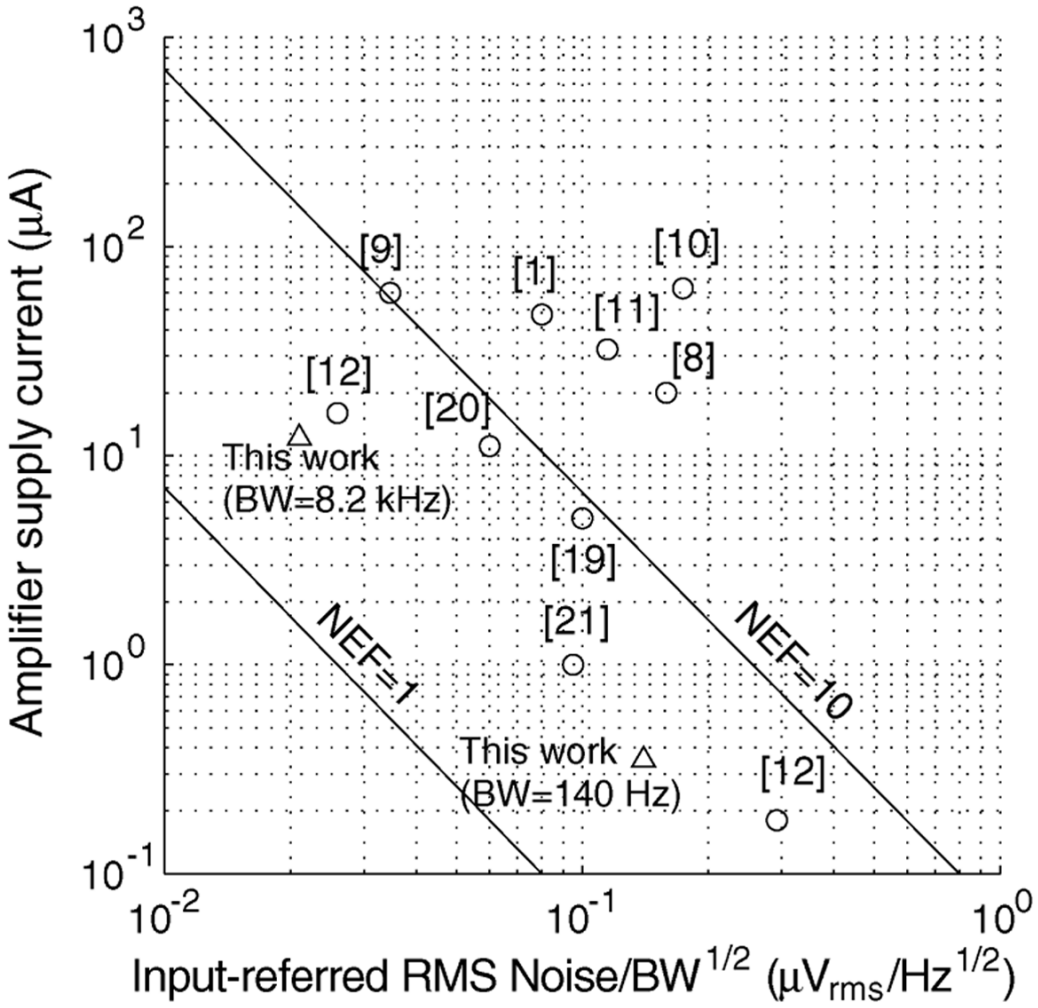

Fig. 7.
Comparison of NEF between the presented amplifier (at two bandwidth settings, BW) and other designs in the literature.

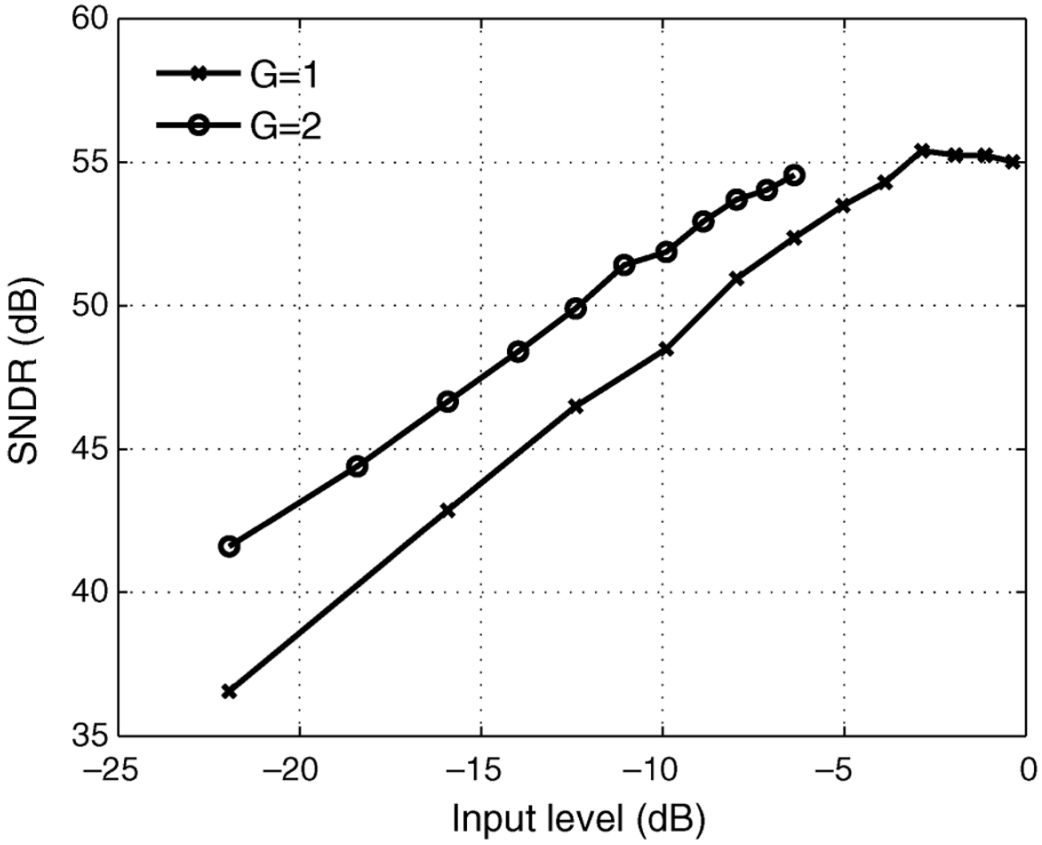

Fig. 8.
Measured SNDR of the ADC for $G = 1$, and OSR = 10. Input level is relative to full scale (125 mV_p sine wave input to the ADC).

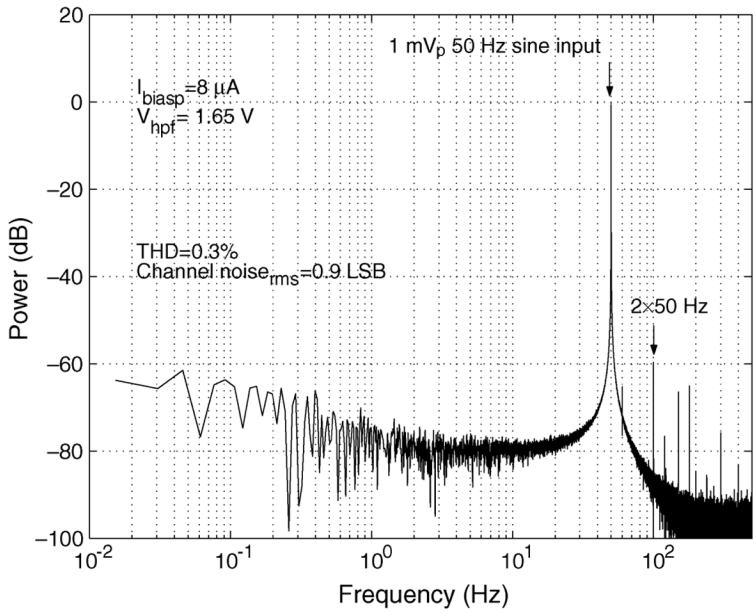

Fig. 9.
Normalized power spectrum of digital output for 1 mV_p 50 Hz sine input to the frontend amplifier.

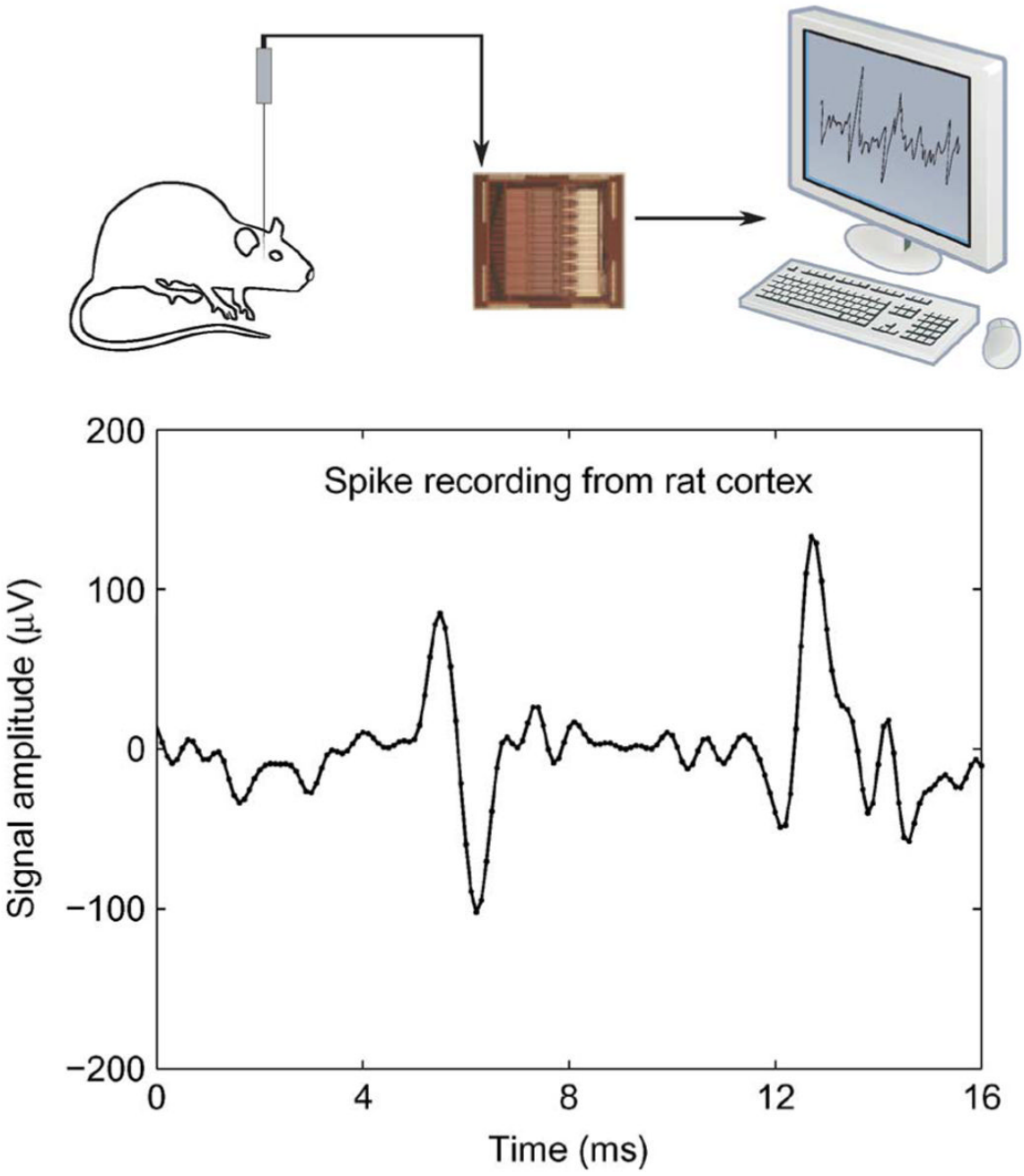

Fig. 10.
In-vivo neural signal recording. Spikes were recorded from rat somatosensory cortex using a tungsten electrode. A screw electrode was used as signal ground.

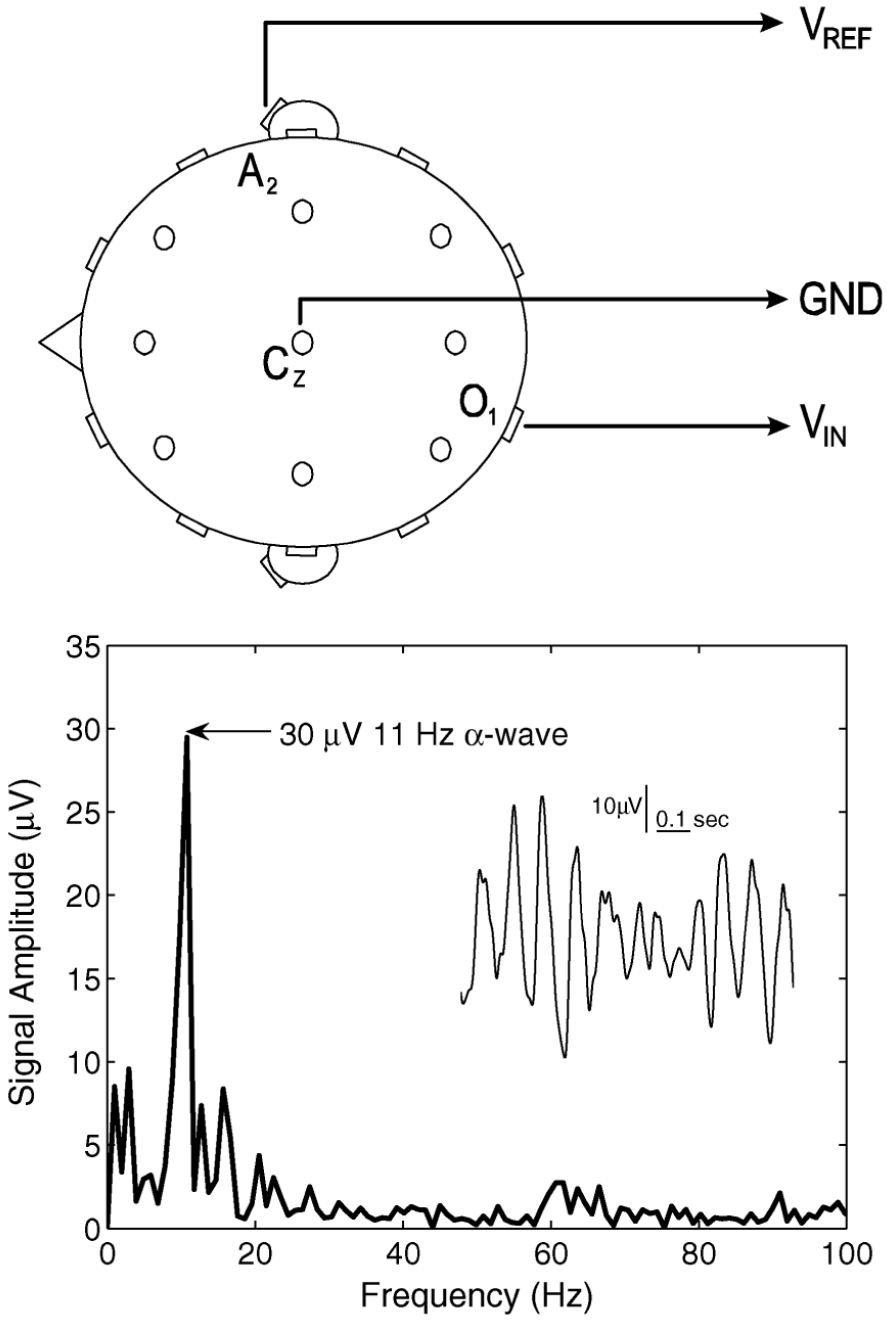

Fig. 11.
Experimental setup for EEG recording and recorded waveform from occipital lobe, with the subject's eyes closed, showing alpha wave activity.

TABLE I

Chip Summary and Measured Characteristics

Technology	AMI 0.5 μm 2P3M CMOS	
Power Supply	3.3 V	
Amplifier	A_v = 39.6 dB	
Lowpass cutoff	140 – 8.2 kHz	
Highpass cutoff	0.2 – 94 Hz	
Bandwidth	8.2 kHz	140 Hz
I_{biasp}	8 μA	100 nA
Input-referred noise	1.94 μV_{rms}	1.65 μV_{rms}
NEF	2.9	3.2
CMRR	> 76 dB (1 Hz – 10kHz)	
PSRR	> 70 dB (1 Hz – 10kHz)	
ADC		
Digital gain	1 – 4096	
Sampling rate	≤ 16 kS/s	≤ 500 S/s
Resolution	7b	12b
Supply current	≤ 23 μA	≤ 23 μA
Channel Total		
THD	≤ 1% (V_{in} ≤ 10 mV_{pp})	
Output noise	< 1 LSB	
Chip Total	16 channels	
Power consumption (maximum)	1.8 mW	
Die size	3mm × 3mm	